Electrically Tunable Plasmonic Behavior of Nanocube–Polymer Nanomaterials Induced by a Redox-Active Electrochromic Polymer

Tobias A. F. König,[†] Petr A. Ledin,[†] Justin Kerszulis,[‡] Mahmoud. A. Mahmoud,[§] Mostafa A. El-Sayed,[§] John R. Reynolds,[†,‡] and Vladimir V. Tsukruk[†,*]

[†]School of Materials Science and Engineering, Georgia Institute of Technology, Atlanta, Georgia 30332-0245, United States, [‡]School of Chemistry and Biochemistry and Center for Organic Photonics and Electronics, Georgia Institute of Technology, Atlanta, Georgia 30332-0400, United States, and [§]Laser Dynamics Laboratory, School of Chemistry and Biochemistry, Georgia Institute of Technology, Atlanta, Georgia 30332-0400, United States

ABSTRACT We present a plasmon-active hybrid nanomaterial design with electrochemical tunability of the localized surface plasmon resonances. The plasmonic-active nanostructures are composed of silver nanocube aggregates embedded into an electrochromic polymer coating on an indium tin oxide electrode with the nanocube aggregation controlled by the surface pressure. Such polymer–nanocube hybrid nanomaterials demonstrated unique tunable plasmonic behavior under an applied electrochemical potential. A significant reversible experimental peak shift of 22 nm at an electrical potential of 200 mV has been achieved in these measurements. Finite-difference time-domain (FDTD) simulations show that, under full oxidation potential, a maximal spectral shift of *ca.* 80 nm can be potentially achieved, which corresponds to a high sensitivity of 178 nm per refractive index unit. Furthermore, FDTD modeling suggests that the electrochemically controlled tunability of plasmonic peaks is caused by reversible changes in the refractive index of the electrochromic polymer coating caused by oxidation or reduction reactions under external electrical potential. Consequently, we define the orthogonal plasmonic resonance shift as a shift that is orthogonal to the redox process responsible for the refractive index change. On the basis of these results, we suggest that the combination of anisotropic nanostructures and electrochromic matrix has the potential to reversibly electrically tune plasmonic resonances over the full visible spectrum.

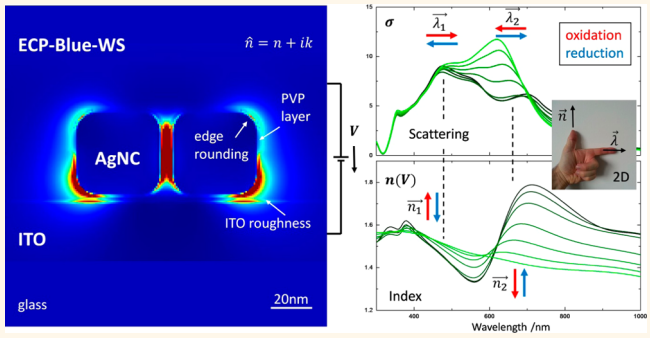

KEYWORDS: localized surface plasmon resonances · electrochromic polymer · electroactive materials · tunable plasmonic behavior · bottom-up assembly

Noble metallic nanoparticles and complex nanostructures made of silver or gold are outstanding building blocks in the design of optical sensors or optical absorbers based on localized surface plasmon resonance (LSPR).[1,2] Significantly higher sensitivity and stronger electromagnetic field enhancement are reported when two noble metallic nanoparticles are in close contact with one another as opposed to a single particle.[3,4] Recent studies have shown that the strong localized plasmonic fields are of interest for applications spanning surface-enhanced Raman scattering (SERS),[5,6] optoelectronics,[7] photovoltaics,[8] and nanophotonics.[9] In order to enable the optical performance of plasmonic nanostructures, it is necessary to tune the peak position, width, and amplitude. In the absence of intimate contact with a substrate (*e.g.*, in dilute solution), the peak position of the plasmonic resonance can be tuned by the nanoparticle size,[10] shape,[11] composition,[12] and refractive index of the surrounding medium.[13] Considering the medium, responsive dielectric environments composed of pH-sensitive polymers,[14,15] light-sensitive materials,[16] photochromic molecules,[17] or conducting polymers[18] are promising candidates for tuning the plasmonic resonance of nanostructures for controlled catalytic events,[19] mapping

* Address correspondence to vladimir@mse.gatech.edu.

Received for review March 22, 2014 and accepted May 28, 2014.

Published online May 28, 2014
10.1021/nn501601e

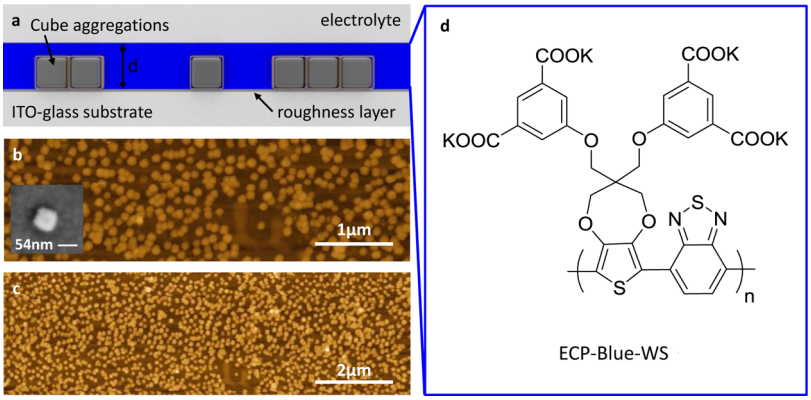

Figure 1. Experimental setup and AFM and SEM images of silver nanocube aggregations as an LB monolayer on an ITO-glass substrate. The 54 nm cubes are covered with a layer of water-soluble electrochromic polymer (ECP-Blue-WS) in an electrolyte solution. A 2 nm roughness value was used to account for the rough ITO surface (a). AFM images of a monolayer of silver nanocubes at different magnifications (b, c) (SEM image inset in (b)). Chemical structure of the ECP-Blue-WS repeat unit (d).

chemical gradients,[20] and modulating plasmonic resonances.[21]

In the case of plasmonic nanostructures integrated on solid substrates (*e.g.*, metal or oxide electrodes), close contact might result in hybridization of the dipolar plasmonic mode into the antibonding mode (at lower energy) and bonding mode (at higher energy).[22] Importantly, the antibonding mode that is related to the electromagnetic field facing away from the substrate causes an improvement in the refractive index sensitivity of the surrounding medium.[23] As it has been suggested, the plasmon peak splitting of the hybridized modes can be controlled by varying the refractive index of the surrounding medium and supporting substrate.[13] Consequently, for the optical design of nanostructures on solid substrates, two challenges should be carefully considered: the ability to precisely fabricate a large number of identical nanoparticle assemblies and the precise characterization of the local enhanced field, which is a nontrivial task for complex aggregates and shapes.[24]

Among the many different approaches for the assembly of nanostructures, the Langmuir–Blodgett (LB) technique enables formation of molecular monolayers at the air–water interface with controlled surface density and local packing.[25] Furthermore, these Langmuir monolayers can be transferred onto solid substrates to allow fabrication of ultrathin solid films.[26] In our previous studies, the LB technique has been used for the preparation of graphene-oxide membranes,[27] the assembly of a variety of amphiphilic macromolecules[28] and branched silsesquioxane-based compounds.[29] Furthermore, it has been demonstrated that the LB technique can be employed to fabricate 2D assemblies of nanoparticles with hydrophobic coatings.[30] By varying the surface pressure, it is possible to tune particle surface density and the degree of aggregation of nanoparticles.[31] There have been recent reports in the characterization plasmonic phenomena with high-resolution spectroscopic methods.[32,33] These optical characterization techniques, combined with sophisticated modeling, are the basis for the understanding of nonlinear local plasmonic effects such as electric field enhancement,[13] surface plasmon interference,[34] mass transport in photosensitive polymers,[35] and shape change in coupled nanoparticle systems.[36,37] However, real-time and reversible tunability of plasmon behavior of metal nanoparticle aggregates has not been achieved.

Herein, we demonstrate electrically tunable plasmonic hybrid nanostructures of silver nanocube aggregates combined with a conjugated electrochromic polymer (ECP) with large and reversible shifts of the plasmonic resonances. In clear contrast to earlier studies, where the enhanced plasmonic sensitivity was based on passive dielectric refractive index changes in chemical environmental composition, we introduce a novel electrically tunable nanocube–polymer nanostructure with reversible tuning of plasmonic properties. These hybrid materials demonstrate spectacular multicyclical reversible tunability of plasmonic optical properties (absorbance and scattering) with an orthogonal plasmonic resonance shift. A silver nanocube LB monolayer that is coated with an electrochromic polymer enables reversible refractive index variation under variable electrical potential, which causes reversible shifts in plasmon resonance peak positions of silver nanocubes (Figure 1). Electrochemical tunability studies with a combination of *in situ* spectroscopic measurements and finite-difference time-domain (FDTD) simulations suggest that the significant plasmonic resonance shifts are triggered by the relative variations of the environmental refractive index of the ECP coating caused by externally controlled and reversible electrochemically driven oxidation and reduction reactions.

RESULTS AND DISCUSSION

Assembly of Silver Nanocubes on an Indium Tin Oxide (ITO) Electrode *via* the LB Method and Polymer Coating. The properties of nanoparticle LB films depend strongly on

preparation and transfer conditions. It was previously demonstrated that as the monolayer of silver nanocubes is compressed on an air−water interphase, the film undergoes transition from gas phase (with large interparticle spacing), through a condensed liquid phase, to a solid phase in which the nanocubes aggregate and form a close-packed superlattice.[38,39] The nanocube monolayer was fabricated by carefully spreading the chloroform solution over the water-filled LB trough and compressed to a desired surface pressure after evaporation of the organic solvent and equilibration. In order to facilitate limited nanocube aggregation, we performed the transfer of the nanocube monolayer at the condensed liquid phase. The surface pressure range, corresponding to the condensed liquid phase, was found from the pressure *vs* surface area isotherm, obtained in a separate experiment (see Figure S1).[40] Then, the nanocube monolayer was transferred onto precleaned ITO electrodes by pulling the ITO substrate up vertically through the air−water interphase while maintaining the constant surface pressure. As can be seen from AFM images of a resulting monolayer, the silver nanocubes were mainly present as individual nanocubes and small aggregates on the surface of the ITO electrode (Figure 1). The surface pressure-dependent aggregation of silver nanocubes affects the optical properties of monolayers, and for further studies we selected 8 mN/m with a modest aggregation level (Figure S2).

Next, an aqueous solution of a water-processable poly(3,4-propylenedioxythiophene-*co*-4,7-benzothiadiazole) ECP was directly spin-cast on top of the LB monolayer deposited on the ITO electrode (Figure 1 and Experimental Section). Due to the characteristic color (blue) and water processability (water solvable, WS) of the ECP, we term this material ECP-Blue-WS. It is important to note that the LB monolayer has sufficiently strong adhesion to the electrode to tolerate spin coating of polymeric solutions from polar and nonpolar solvents such as water and toluene. The polymer film was then rendered insoluble by protonation with *p*-toluenesulfonic acid (PTSA) (1 mg/mL in MeOH).[53] Electrode−nanocube−ECP assemblies with three different thicknesses of the polymer layer (d = 25, 55, and 120 nm) were obtained by varying the concentration of the polymer solution (Figure 1). This allowed us to study three different scenarios: polymer partially covering the sides of the silver nanocubes, polymer fully covering the sides of the nanocubes, and polymer completely covering all surfaces of the nanocubes.

Spectroelectrochemistry of Nanocubes Embedded in Polymer Coatings. The protonated ECP-Blue-WS film undergoes electrochemical switching between a blue-colored, neutral and a transmissive oxidized state.[53] The typical applied potential at which the polymer is completely oxidized in a supporting electrolyte is +800 mV (*vs* Ag/AgCl reference; all further potentials are reported to this reference). Due to the low oxidation potential of silver, the spectroelectrochemistry conditions had to be modified to avoid degradation of the silver nanocubes. We first investigated the electrochemical stability of silver cubes assembled on an ITO electrode *via* cyclic voltammetry (CV) using 0.2 M KCl as an electrolyte and observed a rapid oxidation of silver at potentials exceeding 0 V (Figure S3). However, when purified water (conductivity 2 μS/cm) was used without an electrolyte, the onset of silver nanocube oxidation was observed to shift to 260 mV (*vs* Ag/AgCl).[41,42] On the basis of these results, the following cyclic voltammetry and spectroelectrochemistry experiments with silver nanocubes were limited to a range between −200 and +200 mV.

TABLE 1. Experimental and Modeling Results of Monomer Peak (Monomer Bonding Mode and the Transversal Modes) and Aggregation Peak (Longitudinal Mode) Shifts for Systems with Different ECP-Blue-WS Coating Thicknesses[a]

	monomer peak/nm	aggregation peak/nm
d = 25 nm	1.8 ± 0.6	n/a
d = 55 nm	3.1 ± 1.6	23.7 ± 7.1
d = 120 nm	4.2 ± 1.1	5.3 ± 1.1
AgNC only	1.2 ± 0.4	1.7 ± 1.8
modeled 0−200 mV	2.6	22.0
modeled 0−800 mV	10.4	78.0

[a] Experimental data are averaged over 11 cycles.

As a control experiment, we studied the plasmonic resonance shift as a function of applied potential without a polymer layer in water (Table 1). When the applied potential was cycled between −200 and +200 mV, the monolayer of nanocubes did not show a significant shift of the plasmon peaks. We define the silver nanocube monomer peak in the UV spectra around 440 nm as an overlap between the monomer bonding mode and the transversal modes (dimer and trimer) (Figure 2). The aggregation peak at 620 nm describes the longitudinal mode from the dimer and trimer only. The UV−vis absorbance spectrum of the silver cubes on the ITO electrode was unchanged after as many as 11 electrochemical cycles (Figure S4).

The refractive index change during redox switching of the ECP-Blue-WS has a profound influence on the position of both the monomer and aggregation peaks. Figure 2 shows the UV−vis spectra corresponding to one reduction and oxidation cycle where the applied potential was cycled between −200 and +200 mV in 100 mV increments. Electrochemical oxidation of a 55 nm thick polymer layer over the nanocubes resulted in a 3 nm red shift of the monomer peak and 24 nm blue shift of the aggregation peak (red shift from 449 to 446 nm and blue shift from 608 to 633 nm). These findings match with the behavior predicted from FDTD simulations (summarized in Table 1). An electrochemical reduction results in a reversible

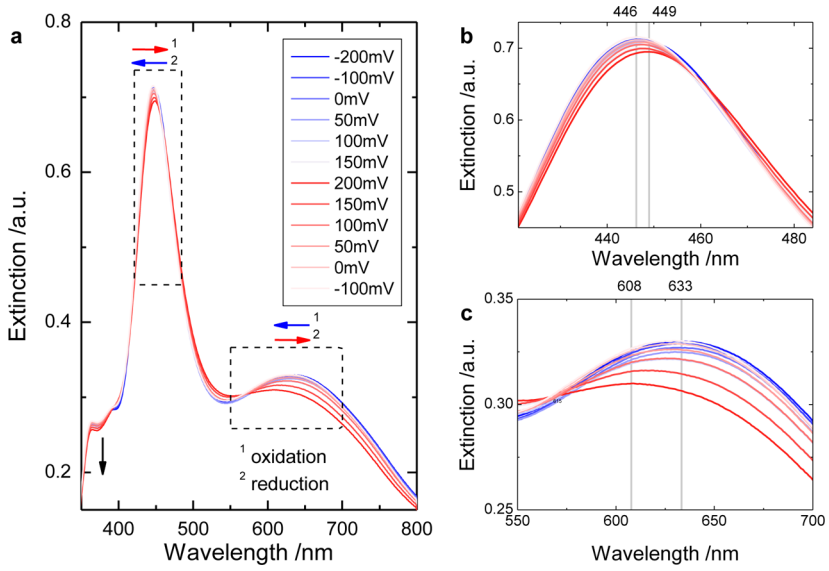

Figure 2. Experimental demonstration of reversible plasmonic shifts of silver nanocubes covered with ECP-Blue-WS under electrochemical oxidation and reduction of polymer coating (d = 55 nm) (a). UV−vis spectra of one switching cycle: (b) monomer peak and (c) aggregation peak. Red and blue arrows indicate the opposite plasmonic resonance shifts upon electrochemical oxidation.

plasmonic resonance shift. With an intermediate layer thickness of 55 nm, we found a good agreement with the theoretically predicted shifts (Table 1). In contrast to the aggregation peak, the monomer peak shows no overlap with ECP peak and is much easier to identify. It is worth noting that only the polymer in close contact with the nanocube contributes to a plasmonic resonance shift, because of the well-known exponential decay of the SPR field.[43]

The reversibility of plasmonic shifting when using an ECP is illustrated in Figure 3. The reversible switching behavior was observed for as many as 11 cycles accompanied by a gradual drift of peak position. This long-term drift can be explained by swelling of the ECP, which results in an increase of the refractive index of the medium, which is also consistent with the direction of the plasmon peak drift.[55] Importantly, there is over an order of magnitude increase of water conductivity to 43 μS/cm after the experimental electrochemical cycling, most likely due to the leaching of entrapped ions from the polymer film. As the polymer contains bound anions (in essence it is "self-doped"), this switching in such a low-conductivity electrolyte is fortuitous. Examination of long-term switching stability of similar structures (beyond 10 cycles demonstrated here) will be a subject of forthcoming studies.

We observed that an increase in polymer thickness does not result in an increase of the plasmonic resonance shift. The aggregation peak is an overlap between the polymer (absorption only) and the plasmonic resonance (absorption and scattering). Experimentally, we observed only the integrated extinction cross-section, which makes a clear identification of the aggregation peak shift difficult.

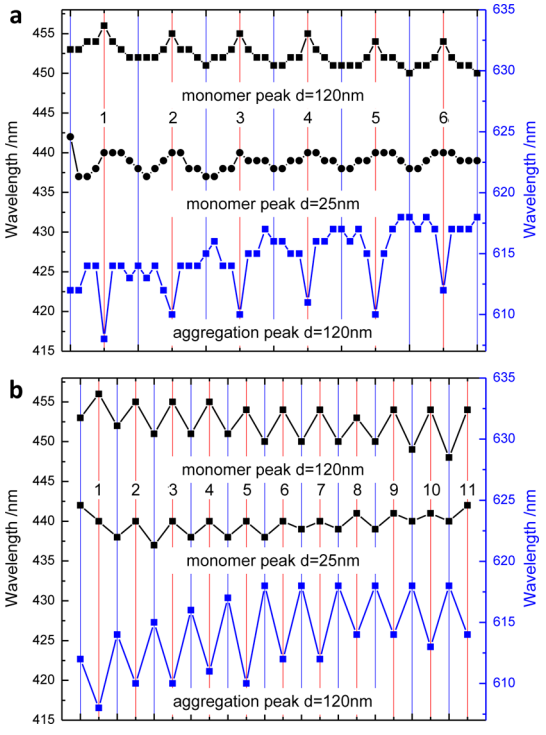

Figure 3. Reversible plasmonic peak shift of silver nanocubes coated with ECP-Blue-WS (d = 25 and 120 nm) during electrochemical oxidation and reduction of the ECP. (a) First six cycles in 100 mV increments. (b) Cycling with maximum and minimum potentials (+200 and −200 mV). Vertical blue and red lines mark −200 and +200 mV data points, respectively. Numbers on red lines denote the cycle number.

Plasmon-Active Nanostructure: Experiment and Modeling Approaches. Statistical analyses of AFM images support the UV−vis observation that the dominant plasmonic peak is originated by individual nanocubes and

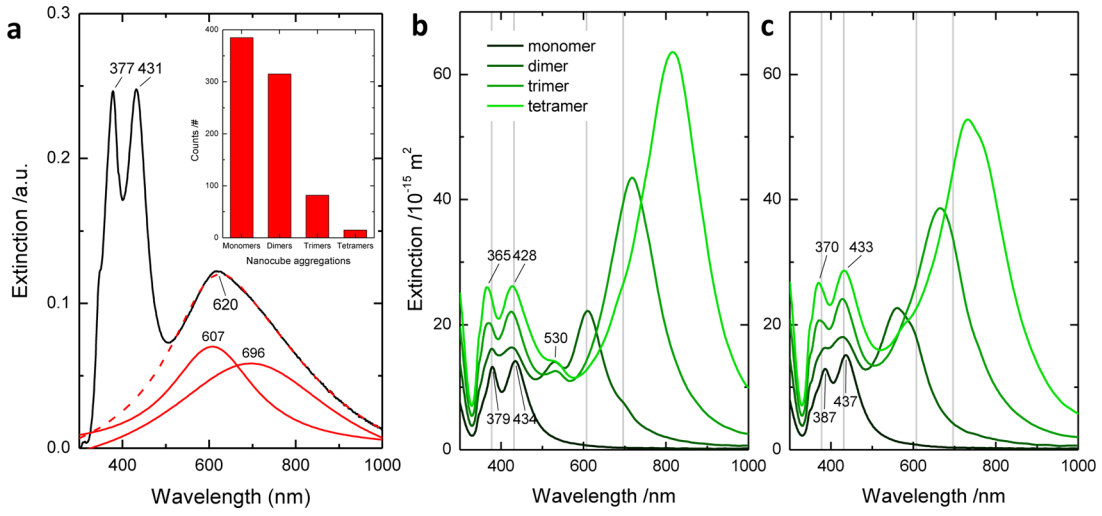

Figure 4. Properties of silver nanocube aggregates on an ITO electrode in air. Experimentally measured extinction cross-section, deconvolution of the aggregation peaks, and statistical distribution of nanocube aggregations (a). Modeled cross-sections of different cube aggregations at 2/4 nm interparticle distance and 1/2 nm PVP coating thickness, respectively (b, c).

nanocube dimers and trimers (Figure 4a). On the basis of the interpretation of the UV−vis extinction cross-section, we indeed observe a dominant monomer peak split (377 and 431 nm) and an aggregation peak at around 620 nm for an LB monolayer of silver nanocubes on the ITO-glass substrate. Due to the presence of the substrate, the monomer peak splits into an antibonding (377 nm) and bonding mode (431 nm) due to the high refractive index of the substrate (ITO, about $n = 2.03 \pm 0.01$ at 400 nm wavelength), relatively large cube size, and relatively sharp cube edges.[13] The aggregation peak, which consists of the longitudinal mode from dimer and trimer clusters, can be deconvoluted into two Lorentzian peaks at 607 and 696 nm.

FDTD modeling reproduced all major experimental plasmonic resonances (Figure 4b,c). The good reproducibility is based on accurate statistical cube size determination and the accurate measurement of the poly(vinylpyrrolidone) (PVP) and ITO refractive index (see Experimental Section). Figure 4b and c shows the simulation results for 1 and 2 nm PVP layer thickness, respectively. The particle aggregation setup is programmed as followed: a PVP layer thickness of 1 nm (2 nm) results in an interparticle distance of 2 nm (4 nm). As expected, an increase of the interparticle distance and increase of the PVP layer thickness result in a blue shift of the longitudinal mode and a slight decrease of extinction cross-section intensity, respectively.[36] This relationship is also known as the plasmon ruler model.[44] Furthermore, the monomer peaks show a slight red shift due to the increase of the PVP layer thickness.[55] The PVP thickness calculations are in agreement with the experimental findings, shown by the highlighted experimental peak positions in Figure 4 (gray solid line). Due to the lack of experimental evidence for resonance splitting of the peak at 530 nm,[45] which we observe only theoretically at an interparticle distance of 2 nm, we chose a PVP layer thickness of 2 nm for further simulations (corresponds to a 4 nm interparticle spacing).

The complex material system studied here consists of a BK7 glass substrate, a 72 nm ITO layer, silver nanocubes covered with PVP, an ECP-Blue-WS layer, and electrolyte solution (aqueous). The refractive index was either taken from the literature or determined by spectral ellipsometry measurements (see Experimental Section). As known, the complex relative permittivity, ε, is related to the refractive index, n:[46]

$$\varepsilon = \varepsilon_r + i\varepsilon_i = (n + ik)^2 \quad (1)$$

To determine the complex refractive index of the ECP-Blue-WS under electrochemical oxidation, we used the refractive index acquired from spectral ellipsometry combined with UV−vis extinction spectra (Figure 5).[53] The UV−vis extinction spectrum can be presented as a superposition of five Lorentzian oscillators (index j = 1−5) and a pole magnitude (Figure 5b). The pole magnitude represents an additional oscillator outside the observation range, which is a Lorentz oscillator with zero broadening.[47] Consequently, the ECP-Blue-WS can be described by (eV units)[46]

$$\varepsilon(E) = \varepsilon_1 + \sum_{5}^{j=1} \frac{A_j w_j E_j}{E_j^2 - E^2 - i w_j E_j} + \frac{M}{E'^2 - E^2} \quad (2)$$

whereby ε_1 = 2.815 denotes the real permittivity constant of the ECP-Blue-WS, A_j the peak amplitude, w_j the peak width, E_j the oscillator position, E' = 0 eV the pole position, and M = 2.506 eV^2 the pole magnitude. The complex refractive index (n and k) for the ECP-Blue-WS is presented in Figure S5.

To determine the complex permittivity under an applied voltage, we used the peak characteristics (peak position, width, and amplitude) from the UV−vis

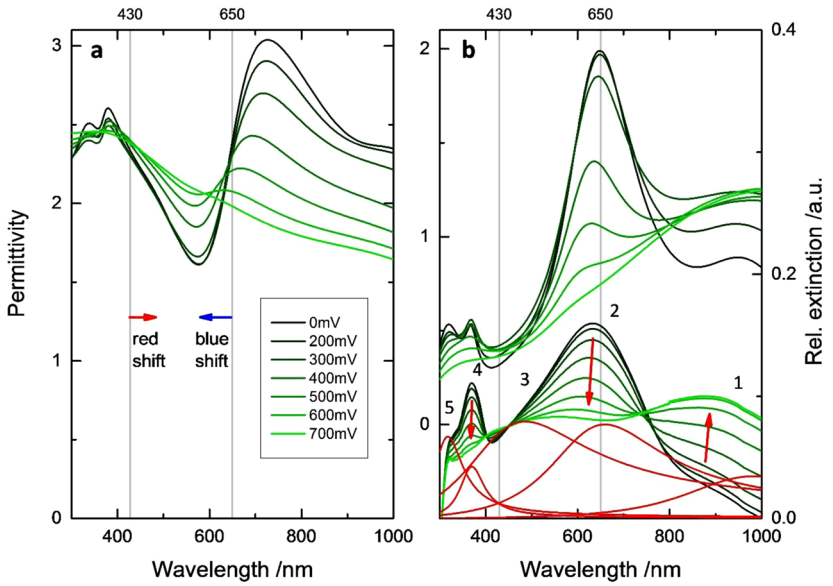

Figure 5. Real permittivity (a), imaginary permittivity, and corresponding relative extinction of the ECP-Blue-WS (b) under different potentials: red shift at 430 nm and blue shift at 650 nm. Red arrows at the extinction cross-section indicate the absorption change during oxidation. The relative extinction is described by a superposition of five Lorentzian functions (red curves).

extinction spectra measured under electrochemical oxidation (Table S1). As a starting value for eq 2, we used values from a separate spectral ellipsometry measurement for an independently prepared ECP-Blue-WS coating on a silicon wafer in air. It is important to note that it is not possible to obtain the imaginary permittivity from the UV−vis extinction spectrum directly because the extinction spectrum overlaps with the absorption from the ITO-glass substrate, electrolyte solution, and the ECP-Blue-WS coating. This overlap changes the peak characteristics, which explains a slight difference compared to the imaginary permittivity in Figure 5b. Due to the normalization to the ITO substrate, the strong absorption from the ITO layer at 300 nm results in a reduced intensity of peak number 5 (see also ITO refractive index in Figure S6).

Modeling of Individual Nanocubes under ECP-Blue-WS Oxidation. FDTD modeling explains the tunable plasmonic resonance shifts of the silver nanocubes surrounded by the ECP-Blue-WS coating under electrochemical oxidation conditions (Figure 6). These simulations show that under electrochemical oxidation all ECP peaks are significantly blue-shifted (about 65 nm) and show a significant reduction in absorption, with the exception of peak 5, which retains its position (Table S1). An increase of the surrounding refractive index of the silver nanocube results in a red shift of the plasmonic resonance.[13] This red shift of the plasmonic resonance is shown with an extinction cross-section of a single nanocube surrounded by air and water located on an ITO substrate (Figure 6). As expected, the higher sensitivity of the antibonding mode results in a more significant red shift (from 386 to 435 nm) compared to the bonding mode (from 437 to 479 nm).

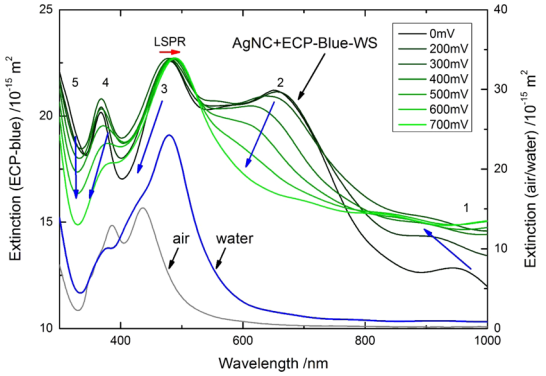

Figure 6. Simulated oxidation of ECP-Blue-WS coating a single silver nanocube (from black to light green lines). The blue arrows indicate the peak position and amplitude shift direction of the polymer under oxidation. The red arrow indicates the opposite plasmon resonance shift under oxidation. Extinction cross-sections of the same nanocube monomer surrounded by air (gray line) and water (blue line).

Consequently, the antibonding mode appears in water as a left shoulder at shorter wavelength (435 nm). From the resonance shift of the bonding mode in Figure 6, we can also determine the refractive index sensitivity of the silver nanocubes on the ITO substrate to be 126 nm/RIU. This sensitivity corresponds to the reported values reported for 60 nm Ag nanocubes on glass.[48] It is worth noting that the plasmonic resonance shift is assumed to be linear with refractive index change, as demonstrated in the literature.[49] The plasmonic resonance shifts from 481 to 490 nm correspond to the expected resonance shift according to the sensitivity (Figure 6). Assuming a linear shift during oxidation, we evaluated a 1.3 nm red shift per 100 mV of applied oxidation voltage for the monomer resonance.

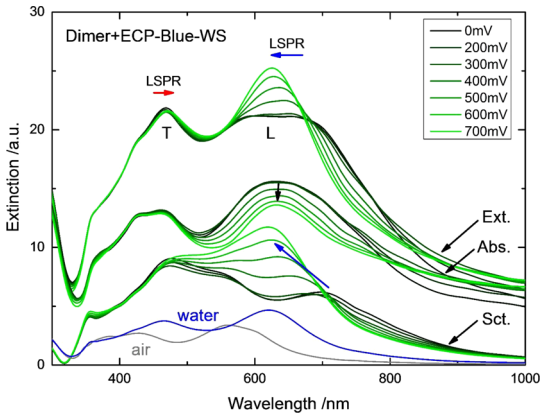

Figure 7. Modeling of ECP-Blue-WS oxidation of a silver nanocube dimer induces a red shift of the transverse mode (T) and a blue shift of longitudinal mode (L) with almost equal contributions of absorption and scattering cross-sections at 30 nm ECP coating. Extinction (cross-section intensity adjusted for clarification) of the nanocube dimer surrounded by air (gray line) and water (blue line).

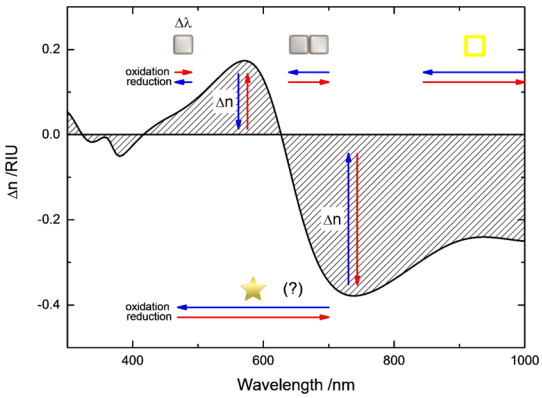

Figure 8. Relative refractive change (Δn) indicates the orthogonal plasmonic resonance shifts. Maximum plasmonic resonance shift of the silver nanocube monomer (arrow length doubled for clarification) and dimer peak, which results in a red and blue shift under oxidation, respectively. Potential resonance shifts of a gold nanoframe and a gold nanostar based on literature values are presented as well.

It can also be seen in Figure 6 that, besides the significant blue shift of the third Lorentzian peak, the plasmonic peak shifts in the opposite direction, which is based on the refractive index change of the polymer. The ECP-Blue-WS absorption can be adjusted by the polymer thickness, but, for demonstration, here we chose a thick polymer layer to obtain an extinction cross-section balance between absorption peaks of the ECP and the plasmonic peaks.

Modeling of Nanocube Aggregates under ECP-Blue-WS Oxidation. To prove the orthogonal plasmonic shift for the aggregated nanocubes, we used a silver nanocube dimer with a 30 nm ECP layer surrounded by water. A thin polymer layer was chosen for the model to attain a good balance between the absorption and scattering cross-section (Figure 7). If we choose a thick polymer layer, we will observe an extinction cross-section dominated by absorption, and it would not be possible to identify the longitudinal mode (aggregation peak). In the same way as for the monomer case, we determined the refractive index sensitivity for the dimer aggregates, which is 105 nm/RIU for the transverse mode and 178 nm/RIU for the longitudinal mode.

Comparing the sensitivities of a transverse mode to a monomer bonding mode, the sensitivity of the transverse mode is about 17% smaller because one cube face is essentially blocked by the second cube; it can be thought that one side is no longer in contact with the medium of interest. A so-called hot spot between the nanocubes is responsible for an enhancement of the electromagnetic field, which results in 42% higher sensitivity as compared to a monomer bonding mode (individual nanocube).[13] According to this refractive index sensitivity, the transverse peak shifts from 428 nm (in air) to 477 nm (in water) and the longitudinal peak shifts from 562 nm (air) to 700 nm (water) due to the refractive index change from air to water (Figure 7).

The scattering cross-section presented in Figure 7 reveals the orthogonal plasmonic shift behavior induced by the relative refractive index change: the red shift for the transversal mode and blue shift for the longitudinal mode. Furthermore, the change in refractive index can also be seen from the absorption cross-sections (Figure 7). Modeling shows a 78 nm blue shift of the longitudinal plasmonic resonance from 697 to 619 nm under full oxidation of the ECP (11 nm blue shift per 100 mV). The transverse mode from 468 to 471 nm is much smaller compared to the monomer mode (around 5 nm).

GENERAL DISCUSSION AND CONCLUSIONS

In contrast to previous work, where sensitivity studies were performed on passive dielectric materials (real refractive index) with irreversible changes in environmental refractive properties, we are able to widen the description to a complex refractive index material. The imaginary part describes the absorption of the material, and it is possible to obtain the real part as pole change at the same peak position as the absorption and *vice versa* (Figure 5).

We suggest that the expected plasmonic resonance shift could be extracted from the absorption cross-section and generalized further by an orthogonal plasmonic shift relation (Figure 8). This plot summarizes the principle of the orthogonal plasmonic shifts relative to the ECP-Blue-WS absorption. First, the expected plasmonic resonance follows the principle of causality, which means that the refractive index change results in a plasmonic resonance shift. Furthermore, we assume that the plasmonic resonance shift is linear with refractive index change.[49] Second, on the basis of the Kramer–Kronig relation, the absorption change direction is orthogonal to the plasmonic

resonance shift direction. Thus, an increase (or decrease) in the refractive index is responsible for a plasmonic resonance red (or blue) shift during electrochemical oxidation. Similarly, processes are opposite during the electrochemical reduction process. It is worth noting that the observed (24 nm) and modeled (78 nm) resonance shifts reported in this study could likely be larger in anisotropic and complex nanoparticles with higher refractive index sensitivity such as nanoframes[50] or nanostars.[51] Indeed, the nanoframes have a theoretical determined sensitivity of 620 nm/RIU,[50] which could result in a 155 nm plasmonic shift, with even higher values expected for nanostars with a sensitivity of 670 nm/RIU.[51]

In conclusion, we have demonstrated the theoretical and experimental realization of a novel electrically tunable plasmon-active nanostructure based on an electrochromic polymer and noble metal nanocubes. This hybrid system is composed of silver nanocube aggregates deposited on an ITO electrode with an ECP coating. FDTD modeling shows that the plasmon resonance shift of coated nanocubes is caused by the relative refractive index change of the ECP coating during electro-oxidation. Furthermore, the FDTD modeling and the spectroelectrochemistry studies show that an increase (or decrease) in the refractive index results in a plasmonic red (or blue) shift. The different silver nanocube aggregation levels result in different shifts of individual plasmonic peaks or plasmonic peaks related to the aggregated state of nanocubes. Indeed, we observed orthogonal plasmonic resonance shifts at two independent plasmonic modes at the same electrochemical potential. Under electrochemical reduction we showed the reversibility of this effect and the repeatability over multiple switching cycles. We suggest that this concept may ultimately be used to tune multiple plasmonic resonances over the entire visible spectrum. Furthermore, this concept is particularly interesting for broadband optical tuning of plasmonic resonances with an external electrical field, which could find applications in tunable plasmonic solar cells and tunable sensors.

EXPERIMENTAL SECTION

Silver Nanocube Synthesis. Silver nanocubes (AgNCs) with 54 nm edge length were synthesized using the polyol method as described elsewhere.[40] Briefly, in a 100 mL round-bottom glass flask, 70 mL of ethylene glycol (EG) was heated to 150 °C for 1 h. Then a solution of 0.85 g of poly(vinylpyrrolidone) was dissolved in 10 mL of EG and added to the hot EG. Then 0.4 mL of sodium sulfide (Na_2S) (3 mM) dissolved in EG and 6 mL of 282 mM silver nitrate dissolved in EG were injected into the reaction mixture. The reaction mixture was stirred at 200 rpm and refluxed at 150 °C for 10 min until the solution became opaque. In order to purify the AgNCs, 5 mL of the prepared AgNC solution was diluted with water and centrifuged at 10 000 rpm for 5 min. The precipitated AgNCs were then redispersed in water.

Assembly of AgNCs on ITO Electrodes *via* the LB Method. We utilized a KSV2000 LB minitrough filled with Nanopure water (18.2 MΩ cm) at room temperature. The surface pressure was measured with a Pt Wilhelmy plate attached to a pressure sensor. The ITO electrode (ITO-glass, CG-60IN-CUV, 7 × 50 × 0.7 mm^3, 15−25 Ω/sq) was purchased from Delta Technologies, Ltd. The ITO substrates (cleaned with acetone and by O_2 plasma etching for 1 min, at 100 μTorr (0.13 mbar)) were submerged into a water phase prior to the formation of a monolayer. Five substrates were bundled edge to edge with conductive sides facing in one direction to ensure the uniformity of the AgNC monolayer between the substrates. The same procedure was used for cleaning the quartz slides (CGQ-0640-01, 75 × 25 mm^2). The stock solution of PVP-coated AgNC in water (1 mL) was diluted to 10 mL using deionized water (18.2 MΩ cm) in a conical-bottom glass centrifuge tube. The AgNCs were separated by centrifugation for 30 min at 4000 rpm and subsequently washed in a similar manner with EtOH/H_2O (10 mL, 1/1, v/v) and EtOH (10 mL).

Finally, the residue was suspended in $CHCl_3$ (2 mL) and used within 1 h for LB deposition. The solution of AgNCs in $CHCl_3$ (1 mL) was carefully spread over the water surface, and the monolayer was left for 30 min to allow for evaporation of the organic solvent and equilibration. The Langmuir monolayer of AgNCs was then compressed at a rate of 5 mm/min to reach a surface pressure of 8 mN/m. The monolayer was transferred onto ITO electrodes at the air−water interface by pulling the ITO substrate up vertically at a rate of 1 mm/min. The monolayer was transferred onto a quartz slide at the air−water interface by pulling the substrate up vertically at a rate of 1 mm/min at surface pressures of 1, 4, 8, and 12 mN/m. The nonconductive side and the edges of the ITO slides were carefully wiped off to remove deposited monolayer with acetone. All samples were stored in a vacuum desiccator.

The electrodes with AgNC monolayer were characterized with UV−vis spectroscopy (Shimadzu UV-2450 spectrophotometer over a wavelength range of 300−1000 nm) and atomic force microscopy (AFM). AFM scanning of the silver nanocubes was conducted using a Digital Instrument Dimension 3000 microscope in tapping mode. Scans were performed with a rate of 0.5−1.0 Hz for surface areas of 5 μm × 5 μm and 10 μm × 10 μm according to the usual procedure adapted in our lab.[52] Silicon nitride tips (MikroMasch) with spring constants of 7 N/m and resonance frequency of *ca.* 150 kHz were used. The AFM images of several different surface areas (5 μm × 5 μm and 10 μm × 10 μm) were collected at a resolution of 512 × 512 pixels. We used the AFM images for statistical analyses (about 800 total counts) of nanocube aggregations.

Electrochromic Polymer Blue (ECP-Blue-WS). All chemical reagents and dehydrated solvents were commercially available and used without further purification unless otherwise noted. All reactions were carried out with oven-dried glassware and dry solvents under an argon atmosphere unless otherwise stated. The synthesis of water-soluble ECP-Blue-WS is reported elsewhere.[53] Briefly, Stille polycondensation was performed between a distannylated-3,4-propylene dioxythiophene monomer and a 4,7-dibromobenzothiadiazole monomer with tris(dibenzylideneacetone)dipalladium and tri(*o*-tolyl)phosphine in degassed toluene and heated at 115 °C for 36 h in an oil bath to afford the organic-soluble ECP-Blue-WS polymer. The organic-soluble polymer was purified by precipitation into methanol and Soxhlet extraction. Hydrolysis of the polymer's ester side chains using 2 M KOH in boiling methanol realized the water-soluble ECP-Blue-WS polymer with high conversion.

Preparation of Polymer-Coated ITO Slides. Aqueous solutions of ECP-Blue-WS (40, 20, and 4 mg/mL) in Nanopure water were used for spin coating onto AgNC-covered slides and bare ITO slides (cleaned as discussed previously). For this study, 120, 55, and 25 nm thick polymer films were obtained by spin coating of 40 and 20 mg/mL solutions at 1000 rpm and a 4 mg/mL solution at 700 rpm, respectively. The resulting films were

allowed to dry under reduced pressure and protonated with *p*-toluenesulfonic acid (1 mg/mL in MeOH) to render the films water-insoluble. The thickness of the polymer films on the ITO electrodes was determined by AFM (specifications see above) profiling as an average of three measurements. The samples were stored in a vacuum desiccator in the dark before use.

Spectroelectrochemistry and Cyclic Voltammetry. Electrochemistry was performed using a three-electrode cell with a platinum wire as the counter electrode, Ag/AgCl as the reference electrode, and an ITO-coated glass slide as the working electrode. All applied potentials are reported *vs* Ag/AgCl. An EG&G Princeton Applied Research model 273 potentiostat was used under the control of CorrWare II software from Scribner and Associates. *In situ* spectroelectrochemistry studies were performed using a Varian Cary 5000 Scan UV−vis/NIR spectrophotometer in water without supporting electrolyte. The electrochemical cell containing water and working and counter electrodes was purged with argon for 5 min. The applied potential steps were 100 mV below 0 V applied potential and 50 mV above 0 V applied potential. The applied potential range was from −200 to 200 mV to avoid silver oxidation. The UV−vis spectra were taken approximately 30 s after applied potential change to allow for current stabilization. For all optical measurements, the spectra were corrected with respect to a reference that included the cuvette, ITO-glass electrode, and water. CV was performed in water under a flow of argon. The scanning rate was 75 mV/s with a sampling interval of 1 mV. Five cycles were performed for each applied potential range (see Figure S3b in the Supporting Information). Water conductivity was measured with a Thermo Orion Star A215 pH/conductivity meter, calibrated with conductivity standards (1.4, 12.9, 119.0 mS/cm) at 22 °C.

Refractive Index Measurements. Spectroscopic ellipsometry measurements were performed with an M-2000U ellipsometer from Woollam Co. The spectral range was 245−1000 nm (D2 and QTH lamps). Ellipsometric data from all samples were acquired at 65°, 70°, and 75° angles of incidence. The refractive index of the ITO-glass slide was determined by using a general oscillator layer with the VASE software (WVASE32 version 3.768). A mean square error (MSE) of 2.23 was obtained at borosilicate glass composition (BK7) from Schott substrate, 72 nm ITO layer, and 2 nm effective medium approximation layer, which accounts for the roughness (see the Supporting Information and Figure S6). The RMS roughness of the ITO layer was 2.8 nm, as determined on 10 μm × 10 μm AFM scans.[54] PVP and ECP-Blue-WS were spin coated at 2000 rpm on a silicon slide precleaned with piranha solution. PVP indexes were fitted with a three-layer model that consists of silicon substrate, silicon oxide layer (1.3 nm layer thickness), and a Cauchy layer (3.13 MSE) (Figure S7). The refractive index of the silicon and silicon oxide was taken from the VASE database.

The ECP-Blue-WS coating properties were analyzed with a three-layer model consisting of a silicon substrate, a 2 nm silicon oxide layer, and a 105 nm general oscillator layer (five Lorentz functions). A reference function was used in the general oscillator layer, which was determined in a separate Cauchy point-by-point fit starting from the longest wavelength (MSE 14.14). Between 300 and 1000 nm the ECP-Blue-WS complex permittivity $\varepsilon(E)$ could be approximated by five Lorentzian functions ($k = 1-5$) and a pole magnitude (Supporting Information). Peak E_k values were determined from a five Lorentzian function fit of the UV−vis extinction spectra of the ECP-Blue-WS coating on a transparent substrate. All extinction spectra fits were performed by OriginPro; $R^2 > 0.99$ by Lorentzian fit functions. Fitted peak position values can be found in Table S1. These positions were used as fixed starting values, and restriction to reference function was used to perform the model fit at zero voltage (MSE 14.46). Despite the slightly increased MSE, the five Lorentzian fit functions (15 fitting parameters) still reflect the optical properties of the ECP-Blue-WS well.

FDTD Simulations. Simulations of the extinction spectra were done using commercial software from Lumerical Solutions Inc. (FDTD Solutions, version 8.0.2). The synthesized AgNCs were 54 ± 6 nm, as statistically evaluated using TEM images (Figure S8). The edge-rounding factor is defined as the edge radius scaled by the length of the nanocube edge. For the modeling, the edge-rounding factor was estimated to be 25%. Each washing step induced a blue shift of the dipole resonance, which is based on an increase of the edge-rounding factor (Figure S9). The AgNCs were also covered by a PVP layer (see refractive index in Figure S7), as described in the synthetic procedure, and the coating thickness was statistically determined to be 1.5 ± 0.3 nm.[55] This thickness was chosen as 1 or 2 nm in FDTD simulations due to the integer mesh size limitations. Consequently, the minimum cube-to-cube distances were selected as 2 and 4 nm, respectively. The polymer coating was rounded at the cube edges to the same degree as the silver nanocube for simulations.

For silver permittivity, we used material data from Hagemann *et al.* (CRC approximation).[56] We found a much better agreement with our experimentally measured extinction spectra by using the permittivity from the CRC approximation instead of the more commonly used source from Johnson and Christy (JC).[57] The significant difference between JC and CRC is the lower imaginary part for the JC data. A lower imaginary part results in a narrower LSPR peak with a higher extinction cross-section, but does not change the plasmonic peak location. The higher imaginary part in the permittivity from CRC approximation could be attributed to geometrical effects, as Shalaev *et al.* have reported.[58] For broadband source simulation, the FDTD software approximates the refractive index of the materials by a built-in function. All materials used, fitting parameters, and RMS errors are listed in Table S2 in the Supporting Information. A simulation mesh size of 1 nm was chosen, and the second conformal variant mesh refinement was used. For the best simulation stability, the mesh area was chosen to be 120 nm larger than the existing structure in all three principal directions. All simulations reached the auto shut off level of 10^{-4} before reaching 75 fs simulation time. To obtain the auto shut off level for ECP-Blue-WS as surrounding material, we had to split the wavelength range into two.

Conflict of Interest: The authors declare no competing financial interest.

Acknowledgment. Financial support from the U.S. Department of Energy, Office of Basic Energy Sciences, Division of Materials Sciences and Engineering, under Award DE-FG02-09ER46604 is gratefully acknowledged. We thank the Partnership for an Advanced Computing Environment (PACE) for computer resources. We thank Michael J. Russell and Kevin Fan for statistical analyses of the silver nanocube aggregation.

Supporting Information Available: This material is available free of charge *via* the Internet at http://pubs.acs.org.

REFERENCES AND NOTES

1. Rodríguez-Lorenzo, L.; de la Rica, R.; Álvarez-Puebla, R. A.; Liz-Marzán, L. M.; Stevens, M.; Plasmonic, M. Nanosensors with Inverse Sensitivity by Means of Enzyme-Guided Crystal Growth. *Nat. Mater.* **2012**, *11*, 604–607.
2. Aydin, K.; Ferry, V. E.; Briggs, R. M.; Atwater, H. A. Broadband Polarization-Independent Resonant Light Absorption Using Ultrathin Plasmonic Super Absorbers. *Nat. Commun.* **2011**, *2*, 517–524.
3. Hao, E.; Schatz, G. C. Electromagnetic Fields around Silver Nanoparticles and Dimers. *J. Chem. Phys.* **2004**, *120*, 357–366.
4. Talley, C. E.; Jackson, J. B.; Oubre, C.; Grady, N. K.; Hollars, C. W.; Lane, S. M.; Huser, T. R.; Nordlander, P.; Halas, N. J. Surface-Enhanced Raman Scattering from Individual Au Nanoparticles and Nanoparticle Dimer Substrates. *Nano Lett.* **2005**, *5*, 1569–1574.
5. Kodiyath, R.; Wang, J.; Combs, Z. A.; Chang, S.; Gupta, M. K.; Anderson, K. D.; Brown, R. J. C.; Tsukruk, V. V. SERS Effects in Silver-Decorated Cylindrical Nanopores. *Small* **2011**, *7*, 3452–3547.
6. Ko, H.; Chang, S.; Tsukruk, V. V. Porous Substrates for Label-Free Molecular Level Detection of Nonresonant Organic Molecules. *ACS Nano* **2009**, *3*, 181–188.

7. Link, S.; El-Sayed, M. A. Spectral Properties and Relaxation Dynamics of Surface Plasmon Electronic Oscillations in Gold and Silver Nanodots and Nanorods. *J. Phys. Chem. B* **1999**, *103*, 8410–8426.
8. Ferry, V. E.; Sweatlock, L. A.; Pacifici, D.; Atwater, H. A. Plasmonic Nanostructure Design for Efficient Light Coupling into Solar Cells. *Nano Lett.* **2008**, *8*, 4391–4397.
9. Tao, A. R.; Ceperley, D. P.; Sinsermsuksakul, P.; Neureuther, A. R.; Yang, P. Self-Organized Silver Nanoparticles for Three-Dimensional Plasmonic Crystals. *Nano Lett.* **2008**, *8*, 4033–4038.
10. Haynes, C. L.; Van Duyne, R. P. Nanosphere Lithography: A Versatile Nanofabrication Tool for Studies of Size-Dependent Nanoparticle Optics. *J. Phys. Chem. B* **2001**, *105*, 5599–5611.
11. Lee, K.-S.; El-Sayed, M. A. Dependence of the Enhanced Optical Scattering Efficiency Relative to That of Absorption for Gold Metal Nanorods on Aspect Ratio, Size, End-Cap Shape, and Medium Refractive Index. *J. Phys. Chem. B* **2005**, *109*, 20331–20338.
12. Wang, H.; Brandl, D. W.; Le, F.; Nordlander, P.; Halas, N. J. Nanorice: A Hybrid Plasmonic Nanostructure. *Nano Lett.* **2006**, *6*, 827–832.
13. König, T.; Kodiyath, R.; Combs, Z. A.; Mahmoud, M. A.; El-Sayed, M. A.; Tsukruk, V. V. Silver Nanocube Aggregates in Cylindrical Pores for Higher Refractive Index Plasmonic Sensing. *Part. Part. Syst. Charact.* **2013**, *31*, 274–283.
14. Gupta, M. K.; Chang, S.; Singamaneni, S.; Drummy, L. F.; Gunawidjaja, R.; Naik, R. R.; Tsukruk, V. V. pH-Triggered SERS *via* Modulated Plasmonic Coupling in Individual Bimetallic Nanocobs. *Small* **2011**, *7*, 1192–1198.
15. Kozlovskaya, V.; Kharlampieva, E.; Khanal, B. P.; Manna, P.; Zubarev, E. R.; Tsukruk, V. V. Ultrathin Layer-by-Layer Hydrogels with Incorporated Gold Nanorods as pH-Sensitive Optical Materials. *Chem. Mater.* **2008**, *20*, 7474–7485.
16. König, T.; Goldenberg, L. M.; Kulikovska, O.; Lazar, K.; Stumpe, J.; Santer, S. Reversible Structuring of Photosensitive Polymer Films by Surface Plasmon Near Field Radiation. *Soft Matter* **2011**, *7*, 4174–4178.
17. Baudrion, A.-L.; Perron, A.; Veltri, A.; Bouhelier, A.; Adam, P.-M.; Bachelot, R. Reversible Strong Coupling in Silver Nanoparticle Arrays Using Photochromic Molecules. *Nano Lett.* **2013**, *13*, 282–286.
18. *Handbook of Conducting Polymers*; Skotheim, T. A.; Reynolds, J. R., Eds.; CRC Press: London, 2007.
19. Dai, Z. G.; Xiao, X. H.; Zhang, Y. P.; Ren, F.; Wu, W.; Zhang, S. F.; Zhou, J.; Mei, F.; Jiang, C. Z. *In situ* Raman Scattering study on a Controllable Plasmon-Driven Surface Catalysis Reaction on Ag Nanoparticle Arrays. *Nanotechnology* **2012**, *23*, 335701.
20. Ramaswamy, R.; Shannon, C. Screening the Optical Properties of Ag–Au Alloy Gradients Formed by Bipolar Electrodeposition Using Surface Enhanced Raman Spectroscopy. *Langmuir* **2011**, *27*, 878–881.
21. Zeng, H.; Sun, S. H. Syntheses, Properties, and Potential Applications of Multicomponent Magnetic Nanoparticles. *Adv. Funct. Mater.* **2008**, *18*, 391–400.
22. Zhang, S. P.; Bao, K.; Halas, N. J.; Xu, H. X.; Nordlander, P. Substrate-Induced Fano Resonances of a Plasmonic Nanocube: A Route to Increased-Sensitivity Localized Surface Plasmon Resonance Sensors Revealed. *Nano Lett.* **2011**, *11*, 1657–1663.
23. Sherry, L. J.; Chang, S. H.; Schatz, G. C.; Van Duyne, R. P.; Wiley, B. J.; Xia, Y. Localized Surface Plasmon Resonance Spectroscopy of Single Silver Nanocubes. *Nano Lett.* **2005**, *5*, 2034–2038.
24. Romo-Herrera, J. M.; Alvarez-Puebla, R. A.; Liz-Marzan, L. M. Controlled Assembly of Plasmonic Colloidal Nanoparticle Clusters. *Nanoscale* **2011**, *3*, 1304–1315.
25. Ariga, K.; Yamauchi, Y.; Mori, T.; Hill, J. P. 25th Anniversary Article: What Can Be Done with the Langmuir-Blodgett Method? Recent Developments and Its Critical Role in Materials Science. *Adv. Mater.* **2013**, *25*, 6477–6512.
26. Blodgett, K. B. Films Built by Depositing Successive Monomolecular Layers on a Solid Surface. *J. Am. Chem. Soc.* **1935**, *57*, 1007–1022.
27. Kulkami, D. D.; Choi, I.; Singamaneni, S. S.; Tsukruk, V. V. Graphene Oxide–Polyelectrolyte Nanomembranes. *ACS Nano* **2010**, *4*, 4667–4676.
28. Kodiyath, R.; Choi, I.; Patterson, B.; Tsitsilianis, C.; Tsukruk, V. V. Interfacial Behavior of pH Responsive Ampholytic Heteroarm Star Block Terpolymers. *Polymer* **2013**, *54*, 1150–1159.
29. Gunawidjaja, R.; Huang, F.; Gumenna, M.; Klimenko, N.; Nunnery, G. A.; Shevchenko, V.; Tannenbaum, R.; Tsukruk, V. V. Bulk and Surface Assembly of Branched Amphiphilic Polyhedral Oligomer Silsesquioxane Compounds. *Langmuir* **2009**, *25*, 1196–1209.
30. Tao, A. R.; Huang, J. X.; Yang, P. D. Langmuir-Blodgettry of Nanocrystals and Nanowires. *Acc. Chem. Res.* **2008**, *41*, 1662–1673.
31. Acharya, S.; Hill, J. P.; Ariga, K. Soft Langmuir–Blodgett Technique for Hard Nanomaterials. *Adv. Mater.* **2009**, *21*, 2959–2981.
32. Novo, C.; Funston, A. M.; Pastoriza-Santos, I.; Liz-Marzan, L. M.; Mulvaney, P. Spectroscopy and High-Resolution Microscopy of Single Nanocrystals by a Focused Ion Beam Registration Method. *Angew. Chem., Int. Ed.* **2007**, *46*, 3517–3521.
33. Nelayah, J.; Kociak, M.; Stephan, O.; de Abajo, F. J. G.; Tence, M.; Henrard, L.; Taverna, D.; Pastoriza-Santos, I.; Liz-Marzan, L. M.; Colliex, C. Mapping Surface Plasmons on a Single Metallic Nanoparticle. *Nat. Phys.* **2007**, *3*, 348–353.
34. König, T.; Tsukruk, V. V.; Santer, S. Controlled Topography Change of Subdiffraction Structures Based on Photosensitive Polymer Films Induced by Surface Plasmon Polaritons. *ACS Appl. Mater. Interfaces* **2013**, *5*, 6009–6016.
35. König, T.; Sekhar, Y. N.; Santer, S. Surface Plasmon Nanolithography: Impact of Dynamically Varying Near-Field Boundary Conditions at the Air-Polymer Interface. *J. Mater. Chem.* **2012**, *22*, 5945–5950.
36. Gupta, M. K.; König, T.; Near, R.; Nepal, D.; Drummy, L. F.; Biswas, S.; Naik, S.; Vaia, R. A.; El-Sayed, M. A.; Tsukruk, V. V. Surface Assembly and Plasmonic Properties in Strongly Coupled Segmented Gold Nanorods. *Small* **2013**, *9*, 2979–2990.
37. Combs, Z. A.; Malak, S. T.; König, T.; Mahmoud, M. A.; Chávez, J. L.; El-Sayed, M. A.; Kelley-Loughnane, N.; Tsukruk, V. V. Aptamer-Assisted Assembly of Gold Nanoframe Dimers. *Part. Part. Syst. Charact.* **2013**, *30*, 1071–1078.
38. Tao, A.; Sinsermsuksakul, P.; Yang, P. Tunable Plasmonic Lattices of Silver Nanocrystals. *Nat. Nanotechnol.* **2007**, *2*, 435–440.
39. Mahmoud, M. A.; Tabor, C. E.; El-Sayed, M. A. Surface-Enhanced Raman Scattering Enhancement by Aggregated Silver Nanocube Monolayers Assembled by the Langmuir-Blodgett Technique at Different Surface Pressures. *J. Phys. Chem. C* **2009**, *113*, 5493–5501.
40. Mahmoud, M. A.; El-Sayed, M. A. Comparative Study of the Assemblies and the Resulting Plasmon Fields of Langmuir–Blodgett Assembled Monolayers of Silver Nanocubes and Gold Nanocages. *J. Phys. Chem. C* **2008**, *112*, 14618–14625.
41. Wang, Y. H.; Yang, X. J.; Bai, J.; Jiang, X.; Fan, G. Y. High Sensitivity Hydrogen Peroxide and Hydrazine Sensor based on Silver Nanocubes with rich {100} Facets as an Enhanced Electrochemical Sensing Platform. *Biosens Bioelectron.* **2013**, *43*, 180–185.
42. Sharma, J.; Rocha, R. C.; Phipps, M. L.; Yeh, H. C.; Balatsky, K. A.; Vu, D. M.; Shreve, A. P.; Werner, J. H.; Martinez, J. S. A DNA-Templated Fluorescent Silver Nanocluster with Enhanced Stability. *Nanoscale* **2012**, *4*, 4107–4110.
43. Raether, H. Surface Plasmons on Smooth and Rough Surfaces and on Gratings. *Springer Tracts in Modern Physics*; Springer, 1988; Vol. 111.
44. Jain, P. K.; Huang, W.; El-Sayed, M. A. On the Universal Scaling Behavior of the Distance Decay of Plasmon

Coupling in Metal Nanoparticle Pairs: A Plasmon Ruler Equation. *Nano Lett.* **2007**, *7*, 2080–2088.
45. Grillet, N.; Manchon, D.; Bertorelle, F.; Bonnet, C.; Broyer, M.; Cottancin, E.; Lerme, J.; Hillenkamp, M.; Pellarin, M. Plasmon Coupling in Silver Nanocube Dimers: Resonance Splitting Induced by Edge Rounding. *ACS Nano* **2011**, *5*, 9450–9462.
46. Wooten, F. *Optical Properties of Solids*; Academic Press: New York, 1972; p 52.
47. Sellmeier, W. Zur Erklärung der Abnormen Farbenfolge im Spectrum einiger Substanzen. *Ann. Phys. Chem.* **1871**, *219*, 272–282.
48. Mahmoud, M. A.; El-Sayed, M. A. Effect of the Dielectric Constant of the Surrounding Medium and the Substrate on the Surface Plasmon Resonance Spectrum and Sensitivity Factors of Highly Symmetric Systems: Silver Nanocubes. *J. Am. Chem. Soc.* **2012**, *134*, 6434–6442.
49. Mayer, K. M.; Hafner, J. H. Localized Surface Plasmon Resonance Sensors. *Chem. Rev.* **2011**, *111*, 3828–3857.
50. Mahmoud, M. A.; El-Sayed, M. A. Gold Nanoframes: Very High Surface Plasmon Fields and Excellent Near-Infrared Sensors. *J. Am. Chem. Soc.* **2010**, *132*, 12704–12710.
51. Nehl, C. L.; Liao, H. W.; Hafner, J. H. Optical Properties of Star-Shaped Gold Nanoparticles. *Nano Lett.* **2006**, *6*, 683–688.
52. McConney, M. E.; Singamaneni, S.; Tsukruk, V. V. Probing Soft Matter with the Atomic Force Microscopies: Imaging and Force Spectroscopy. *Polym. Rev.* **2010**, *50*, 235–286.
53. Shi, P.; Amb, C. M.; Dyer, A. L.; Reynolds, J. R. Fast Switching Water Processable Electrochromic Polymers. *ACS Appl. Mater. Interfaces* **2012**, *4*, 6512–6521.
54. Horcas, I.; Fernandez, R.; Gomez-Rodriguez, J. M.; Colchero, J.; Gomez-Herrero, J.; Baro, A. M. WSXM: A Software for Scanning Probe Microscopy and a Tool for Nanotechnology. *Rev. Sci. Instrum.* **2007**, *78*, 013705.
55. Kodiyath, R.; Malak, S. T.; Combs, Z. A.; König, T.; Mahmoud, M. A.; El-Sayed, M. A.; Tsukruk, V. V. Assemblies of Silver Nanocubes for Highly Sensitive SERS Chemical Vapor Detection. *J. Mater. Chem. A* **2013**, *1*, 2677–2678.
56. Hagemann, H. J.; Gudat, W.; Kunz, C. Optical Constants from the Far Infrared to the X-ray Region: Mg, Al, Cu, Ag, Au, Bi, C, and A12O3. *J. Opt. Soc. Am.* **1975**, *65*, 742–744.
57. Johnson, P. B.; Christy, R. W. Optical Constants of the Noble Metals. *Phys. Rev. B* **1972**, *6*, 4370–4379.
58. Drachev, V. P.; Chettiar, U. K.; Kildishev, A. V.; Yuan, H.-K.; Cai, W.; Shalaev, V. M. The Ag Dielectric Function in Plasmonic Metamaterials. *Opt. Express* **2008**, *16*, 1186–1195.